An experimental study of shear-enhanced convection in a mushy layer

JEROME A. NEUFELD[1]† AND J. S. WETTLAUFER[1,2]

[1]Department of Geology and Geophysics, Yale University, New Haven, CT 06520, USA
[2]Department of Physics, Yale University, New Haven, CT 06520, USA

The influence of an external shear flow on the evolution of a solidifying array of dendritic crystals, termed a mushy layer, is investigated through controlled cooling of an aqueous ammonium chloride solution in a laboratory flume. The controlled cooling produces a mushy layer that grows at a constant rate from the base of the flume over which a laminar shear flow is applied. We find a critical flow speed above which a spatiotemporal variation of the solid fraction of the layer appears with a planform transverse to the flow direction. The presence of this distinctive pattern of spanwise crevasses is compared with a simplified stability analysis in which the motion of the external fluid over the corrugated mush–liquid interface produces a pressure perturbation that drives flow and phase change within the mushy layer. This flow leads to a pattern of solidification and dissolution that is compared to the experimental results. The physical mechanism underlying the pattern formation is confirmed by the agreement between the theoretical predictions and experimental results. Finally, the comparison between theory and experiment provides a value for the mushy layer permeability, the evolution of which is of relevance to a host of geophysical, biological and engineering systems.

1. Introduction

Systems in which both fluid flow and solidification play a role are governed by a rich hierarchy of physical processes acting on a wide range of length scales, all of which greatly influence the electrical and mechanical properties of the material so produced (see reviews by Glicksman, Coriell & McFadden 1986; Davis 1990, 2001; Worster 2000). In the case of binary alloys, these material properties are controlled by the processes of solidification which, in many systems of geophysical and metallurgical interest, proceed through the growth of an array of dendritic crystals, termed a mushy layer. Because of the highly convoluted solid–liquid interface, these crystal arrays are often modelled as a reactive porous medium on a length scale larger than the inter-dendrite spacing. In so doing, the volume fraction of solid ϕ, is determined by a thermodynamic coupling between heat and solute (see reviews by Worster 1992a, 2000). In the absence of an external flow variations in concentration and temperature of the interstitial fluid can lead to buoyant instabilities driving fluid flow both within the liquid and within the mushy layer as shown experimentally by Copley *et al.* (1970) and theoretically by Worster (1992b) and Chen, Lu & Yang (1994).

† Present Address: Institute of Theoretical Geophysics, Department of Applied Mathematics and Theoretical Physics, University of Cambridge, Wilberforce Road, Cambridge, CB3 0WA, UK

Convective motions of the liquid within this system can arise due to compositional and thermal gradients both within, and external to, the mushy layer. Convective motions associated with the buoyancy of the interstitial fluid give rise to the so-called mushy layer mode, while the boundary layer mode is associated with the instability of a compositional boundary layer external to the mushy layer, as detailed by Worster (1992b) and Chen *et al.* (1994). Once initiated, flow within the mushy layer advects both temperature and solute leading to local solidification and dissolution. Owing to the sensitive dependence of mushy layer permeability on the solid fraction, flow leading to dissolution becomes rapidly focused in confined regions of zero solid fraction termed 'chimneys'.

The pattern of dissolution characteristic of chimney formation is found in many material systems, and is associated with the formation of defects termed 'freckles' in metallurgy. Models predicting the onset of chimney formation are highly desirable because these patterns are associated with zones of weakness in the resultant material. The formation and dynamics of chimneys has been investigated experimentally in a host of systems by a number of authors. Chen & Chen (1991) first characterized the solid fraction and structure of chimneys in an aqueous system by performing *a posteriori* computed tomography (CT) x–ray scans of mushy layers formed through the cooling of super-eutectic aqueous ammonium chloride (NH_4Cl) solutions. Tait & Jaupart (1989, 1992) explored the formation of chimneys in the NH_4Cl system as a function of both fluid viscosity and mushy layer depth. Huppert, Hallworth & Lipson (1993) investigated the effect of crystallography on permeability through the systematic doping of an NH_4Cl mushy layer with trace concentrations of copper sulphate. More recently, Aussillous *et al.* (2006) used MRI techniques to make *in-situ* measurements of the growth of a mushy layer from an aqueous sugar solution and observed the formation of highly branched chimney structures. Studies that more faithfully reproduce the base state of the linear stability analyses of Worster (1992b) and Chen *et al.* (1994) have been undertaken by Peppin *et al.* (2007) in a directional solidification apparatus. Using this apparatus they were able to characterize not only the growth of the NH_4Cl mushy layer, but also to construct a regime diagram showing the formation of chimneys as a function of bulk concentration and pulling speed.

Motivated in part by the growth of sea ice, the formation of chimneys has been observed in the laboratory by Wettlaufer, Worster & Huppert (1997a, b) using an aqueous sodium chloride solution. They found a critical ice thickness beyond which the rejection of salt associated with the formation of sea ice leads to a buoyant instability driving convective motion within the newly forming mushy layer. This convection rapidly gave rise to the formation of chimneys within the sea ice, and is the principal mechanism by which salt is drained from the ice. They characterized the onset of this convection by a porous-medium Rayleigh number which itself is proportional to both the mushy layer depth and its permeability. For this reason, the onset of convection within sea ice, and the incipient formation of chimneys or 'brine channels', is causally tied to the heat and salt fluxes at the ocean surface which in turn play a large role in determining the hydrography of polar oceans.

Theoretical analyses of the effect of forced flows on the evolution of a mushy layer have been undertaken by Feltham & Worster (1999), Chung & Chen (2001), Neufeld *et al.* (2006) and most recently by Neufeld & Wettlaufer (2008). In their study Feltham & Worster (1999) coupled flow in the melt to the growth of the mushy layer principally through pressure perturbations evaluated at the corrugated mush–liquid interface. They found that, for a sufficiently vigorous far-field velocity, these interfacial pressure perturbations drive flow within the mushy layer that, in turn, perturbs the

isotherms. They concluded that the resultant compression of the isotherms at peaks in the interface and rarefaction at troughs leads to enhanced growth of the interfacial corrugations at wavenumbers commensurate with the depth of the mushy layer. Chung & Chen (2001) extended this analysis to include the effects of buoyancy in both the mushy layer and the overlying liquid. They also found that for sufficiently vigorous external flows corrugations are enhanced, although their analysis predicted a wavelength commensurate with the thickness of the compositional boundary layer. Neufeld & Wettlaufer (2008) re-examined the effect of an external flow on the buoyant convective modes present in the solidifying mushy layer system for a wide range of material parameters. They found that sufficiently vigorous flows will force both the boundary and mushy layer modes. In contrast to previous authors, they interpret the forced boundary layer mode as a translation of the interfacial corrugation and argue that it is the forced mushy layer mode that leads to solidification and dissolution of the matrix.

This paper focuses on the forced mushy layer mode of convection and experimental observations of its dramatic influence on the morphology of the mushy layer. In §2 we review the ideal mushy layer model of Feltham & Worster (1999) and Neufeld *et al.* (2006) and find the steady-state solution in the limits relevant to our experimental system. In §3 we follow their stability analysis of a mushy layer in the presence of a vigourous external flow including, in this instance, the effects of both buoyancy within the mushy layer and dissolution and solidification of the mushy layer. We characterize the relative effects of buoyancy and shear forcing by the external flow, and show that the permeability of the mushy layer plays a crucial role in the forced instability. The experimental apparatus with which the instability is observed and the technique employed to generate steady-state growth of a mushy layer are introduced in §4. Finally, the results of our experiments are compared to the simplified theoretical analysis in §5. General conclusions are presented in §6, along with a discussion of the relevance of the work in metallurgical, biological and geophysical contexts.

2. Theoretical model of forced convection within the mushy layer

2.1. *Formulation of the problem*

In order to ensure that this paper is reasonably self-contained, we review the formulation of Feltham & Worster (1999) and Neufeld *et al.* (2006). The purpose of this review is not simply to compare their results with our experimental results, but to show that a simple extension of their model incorporating both changes in phase and buoyancy effects yields the observed patterns of solidification and dissolution found in our experiments. The model presented here is a simplified treatment of the forced mushy layer mode investigated by Neufeld & Wettlaufer (2008). The model is motivated by the experimental results described in §5 and therefore treats both buoyant and forced convection in an aqueous 28 wt % NH_4Cl mushy layer solidified from below at constant velocity V using 'ideal' mushy layer theory, as shown in figure 1. In 'ideal' mushy layer theory the temperature and concentration of the mushy layer are coupled through the solutally dependent freezing point and differences in the density, diffusivity and specific heat between the liquid and solid are neglected (see reviews by Worster 1992*b*, 2000). Cooling the binary solution from below results in a mushy layer in the region $0 < z < \zeta$ that is bounded from below by solid and above by a semi-infinite liquid solution. The base of the mushy layer is at the eutectic temperature T_E, the point at which a solid solution is formed. Owing to the large interfacial surface area of the highly dendritic crystals comprising
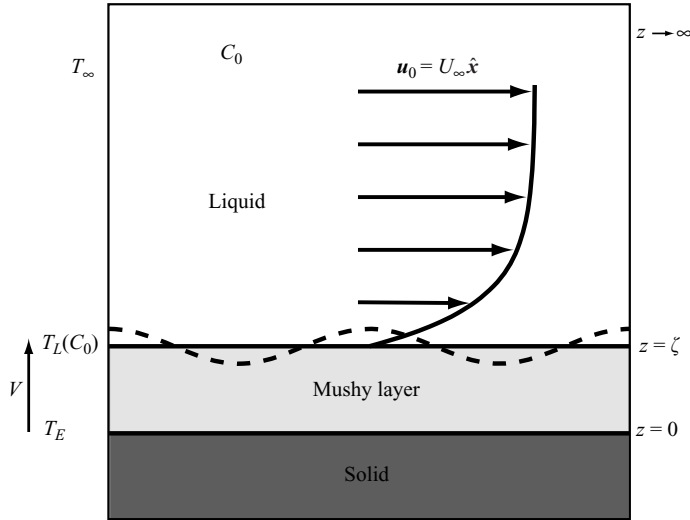
FIGURE 1. Schematic of the system under consideration. A uniform flow is imposed over a growing mushy layer. Flow within the mushy layer is coupled to that in the liquid via a perturbed mush–liquid interface.

the mushy layer, local thermodynamic equilibrium is assumed. Therefore, within the mushy layer the temperature T is related to the solute concentration C through a linear liquidus relationship; $T_L(C) = T_E + \Gamma(C - C_E)$ where Γ is the slope of the liquidus curve (constant over the range of relevance to our work) and C_E is the eutectic concentration. Far from the mush–liquid interface, the temperature in the overlying liquid tends to the far-field value T_∞.

Motivated by the experimental findings detailed in §5 we focus on patterns of solidification and dissolution within the mushy layer. These patterns are a result of the confluence of buoyant and forced fluid motion. Worster (1992b) and Neufeld & Wettlaufer (2008) have shown that convective motions arising solely in the liquid due to the diffusive compositional boundary layer generate negligible flow within the underlying mushy layer and have only a small effect on its morphology. For clarity of presentation we therefore neglect the effects of thermal and compositional variations on buoyancy in the overlying liquid. In addition we neglect diffusion of solute both within the mushy layer and the overlying liquid.

The equations governing the mushy layer shown below have been described in this setting by Feltham & Worster (1999). Here we include the effects of buoyancy within the mushy layer to illustrate the progression from buoyancy- to shear-driven instability as the strength of the external flow is increased. Length, time and pressure are scaled by κ/V, κ/V^2 and ρV^2 respectively, and thus non-dimensional equations expressing conservation of heat and solute within the mushy layer can be written as

$$(\partial_t - \partial_z)(\theta - \mathscr{S}\phi) + \boldsymbol{u} \cdot \nabla\theta = \nabla^2\theta, \qquad (2.1)$$

$$(\partial_t - \partial_z)[(1 - \phi)\theta + \mathscr{C}\phi] + \boldsymbol{u} \cdot \nabla\theta = 0. \qquad (2.2)$$

Here θ is the dimensionless temperature and concentration defined by

$$\theta = \frac{T - T_L(C_0)}{\Delta T} = \frac{C - C_0}{\Delta C}, \qquad (2.3)$$

where $\Delta T = T_L(C_0) - T_E$ and $\Delta C = C_0 - C_E$. The effects of latent heat upon solidification are characterized by the dimensionless Stefan number

$$\mathscr{S} = \frac{\mathscr{L}}{c\Delta T}, \tag{2.4}$$

and the importance of solute rejection is embodied in

$$\mathscr{C} = \frac{C_S - C_0}{\Delta C}, \tag{2.5}$$

where $\mathscr{L}$ is the latent heat, c is the specific heat capacity and C_S is the concentration of the solid.

Importantly, the mushy layer is treated as a porous medium using Darcy's law

$$\boldsymbol{u} = -\Pi_0\nabla p - R_m\theta\hat{\boldsymbol{z}}, \tag{2.6}$$

where the permeability of the mushy layer is characterized by the non-dimensional Darcy number

$$\Pi_0 = \frac{\tilde{\Pi}_0}{(\kappa/V)^2}, \tag{2.7}$$

and in contrast to Feltham & Worster (1999) the effects of both thermal and compositional buoyancy are incorporated through a porous-medium Rayleigh number

$$R_m = \frac{g(\tilde{\beta} - \Gamma\tilde{\alpha})\Delta C\tilde{\Pi}_0(\kappa/V)}{\kappa\nu}. \tag{2.8}$$

Here p is the dynamic pressure, g is the acceleration due to gravity, $\tilde{\alpha}$ and $\tilde{\beta}$ are the thermal and solutal coefficients of expansion respectively and ν is the kinematic viscosity. While the permeability of the mushy layer is, in general, anisotropic and depth dependent (through the solid fraction), we simplify the analysis substantially by considering a locally isotropic dimensional permeability $\tilde{\Pi}_0$ which is, to leading order, constant with depth. We note that the assumption of local isotropy is well satisfied in the NH$_4$Cl system since the resultant mushy layer is composed of an array of closely spaced, predominantly vertical, dendritic structures. While the permeability of the mushy layer is expected to depend on the local solid fraction, which increases with depth into the mushy layer (see §2.2), we have used a constant permeability in comparison with the experimental results of §4 and §5. The permeability used in the following theoretical analysis is therefore best interpreted as a depth-averaged permeability.

Within the overlying liquid, advection and diffusion of heat are modelled by

$$(\partial_t - \partial_z)\theta + \boldsymbol{u}\cdot\nabla\theta = \nabla^2\theta, \tag{2.9}$$

flow is governed by the Navier–Stokes equations

$$(\partial_t - \partial_z)\boldsymbol{u} + \boldsymbol{u}\cdot\nabla\boldsymbol{u} = -\nabla p + Pr\nabla^2\boldsymbol{u}, \tag{2.10}$$

where $Pr = \nu/\kappa$ is the Prandtl number, and by an equation describing conservation of mass

$$\nabla\cdot\boldsymbol{u} = 0. \tag{2.11}$$

The following thermodynamic boundary conditions are imposed;

$$\theta = -1 \quad (z = 0), \tag{2.12a}$$

$$\theta = 0, \quad \phi = 0, \quad [\theta]_l^m = 0, \quad \phi\mathscr{S}v_n = [\hat{\boldsymbol{n}}\cdot\nabla\theta]_l^m \quad (z = \zeta), \tag{2.12b, c, d, e}$$

$$\theta \to \theta_\infty \qquad (z \to \infty). \tag{2.12f}$$

Here $\theta_\infty = [T_\infty - T_L(C_0)]/\Delta T$ is the dimensionless far-field temperature, $\hat{\boldsymbol{n}}$ is the unit normal pointing into the melt, v_n is the normal growth velocity of the interface and $[\ ]_l^m$ denotes a jump in the quantities across the mush–liquid interface. These boundary conditions express the following constraints. The base of the mushy layer is fixed at the eutectic temperature (2.12a) and, owing to our neglect of compositional diffusion within the liquid, the mush–liquid interface is fixed at the liquidus temperature at the bulk concentration (2.12b). The requirement of zero solid fraction at the mush–liquid interface (2.12c) follows from the assumption of marginal equilibrium as discussed by Worster (1986, 2000). We require continuity of both the thermal field (2.12d) and conservation of heat at the mush–liquid interface (2.12e), generally known as the Stefan condition. Finally, the temperature in the overlying liquid asymptotes to its far-field value (2.12f).

The boundary conditions on the fluid velocity are as follows:

$$\boldsymbol{u} = 0 \qquad (z = 0), \tag{2.13a}$$

$$[\boldsymbol{u} \cdot \hat{\boldsymbol{n}}]_l^m = 0, \quad [p]_l^m = 0, \quad [\boldsymbol{u} \times \hat{\boldsymbol{n}}]_l = 0 \qquad (z = \zeta), \tag{2.13b, c, d}$$

$$\boldsymbol{u} \to U_\infty \hat{\boldsymbol{x}} \quad (z \to \infty), \tag{2.13e}$$

where U_∞ is the imposed far-field velocity. Condition (2.13a) requires vanishing velocity at the base of the mushy layer. At the mush–liquid interface (2.13b) and (2.13c) express continuity of mass flux and pressure respectively. In the limit of small mushy layer permeability we use a no-slip condition at the mush–liquid interface (2.13d) rather than the more general Beavers–Joseph boundary condition (Beavers & Joseph 1967). Finally, we require the velocity within the liquid to asymptote to its far-field value (2.13e).

2.2. *Basic steady-state solution*

We briefly review the steady state found by Feltham & Worster (1999) in the limit $\mathscr{C} \gg 1$ and note that in our experiment $\mathscr{C} \simeq 10$. The basic steady state, denoted by subscript zero, describes a stagnant mushy layer ($\boldsymbol{u}_0^m = 0$) with an asymptotic suction profile in the overlying liquid,

$$\boldsymbol{u}_0^l = (u^l, v^l, w^l) = (U_\infty[1 - e^{-(z - \zeta_0)/Pr}], 0, 0), \tag{2.14}$$

where the $\hat{\boldsymbol{x}}$ coordinate has been oriented with the flow as shown in figure 1. The temperature and solid fraction of the mushy layer are given by

$$\theta_0^m = \frac{\theta_\infty}{\Lambda} \left[1 - e^{-\Lambda(z - \zeta_0)} \right], \tag{2.15}$$

$$\phi_0^m = -\frac{\theta_0^m}{\mathscr{C}}, \tag{2.16}$$

where $\Lambda = 1 + \mathscr{S}/\mathscr{C}$. Within the overlying liquid the temperature decays to its far-field value,

$$\theta_0^l = \theta_\infty \left[1 - e^{-(z - \zeta_0)} \right]. \tag{2.17}$$

Therefore, the mushy layer depth, as determined by the Stefan condition (2.12e), is

$$\zeta_0 = \frac{1}{\Lambda} \ln \left[1 + \frac{\Lambda}{\theta_\infty} \right]. \tag{2.18}$$

3. Linear stability analysis

We study the relative importance of buoyancy- and shear-forced convection within the mushy layer through the following linear stability analysis. This work is an extension of the work of Feltham & Worster (1999) and Neufeld *et al.* (2006) that includes the effects of buoyancy and solidification/dissolution of the matrix and a reduced form of the forced mushy layer mode described by Neufeld & Wettlaufer (2008) where both thermal and compositional perturbations were considered in the overlying layer. As shown by Feltham & Worster (1999) thermal perturbations in the liquid only lead to a small translation of the interface while leaving the overall stability of the shear-forced mushy layer mode unaffected. Finally, it is important to note that application of an external flow breaks the symmetry of the purely buoyant problem and hence application of Squire's theorem ensures that the effect of the external flow will be strongest in the flow direction and will have no effect in the cross-stream direction as demonstrated by Chung & Chen (2001). We therefore consider only perturbations to the basic steady state of the typical normal mode form

$$(\theta^m, w^l, w^m, \zeta) = (\theta_0^m, w_0^l, w_0^m, \zeta_0) + (\theta_1^m, w_1^l, w_1^m, \zeta_1)e^{\sigma t + ikx}, \tag{3.1}$$

with wavenumbers k aligned with the external flow, where θ_1^m, w_1^l and w_1^m depend only on the z-coordinate. The problem is further simplified by noting that for most systems of interest the mushy layer permeability is small. In this limit, flow within the overlying liquid can be approximated well by that of a viscous liquid impinging upon a corrugated impermeable medium. The principal effect of the overlying liquid is therefore to induce pressure variations at the mush–liquid interface. These pressure perturbations in turn drive a flow within the underlying mushy layer that, owing to the associated advection of heat and solute within the matrix, results in patterns of solidification and dissolution. In this manner a reduced model is constructed in which the flow of an external liquid over a corrugated interface is coupled with convective flows in a reactive porous medium through a pressure matching condition at the interface. We first solve for the flow of an external liquid over a corrugated interface and find the resultant pressure perturbations at the mush–liquid interface. Both the pressure perturbations and the buoyancy of the interstitial fluid then drive flows within the reactive porous medium.

3.1. *Perturbed flow in the melt*

Flow within the overlying liquid layer is described by a modified Orr–Sommerfeld equation with boundary conditions describing the perturbed interface. We briefly review the solution of the interfacial pressure perturbations found by Neufeld *et al.* (2006) using the formulation of Feltham & Worster (1999). In that formulation, perturbed flow in the melt is given by

$$\left[Pr(D^2 - k^2) + D\right]\left[D^2 - k^2\right]w_1$$
$$= ikU_\infty\left\{\left[1 - e^{-(z-\zeta_0)/Pr}\right]\left[D^2 - k^2\right] - Pr^{-2}e^{-(z-\zeta_0)/Pr}\right\}w_1, \tag{3.2}$$

with boundary conditions

$$w_1 = 0, \quad Dw_1 = ik\frac{U_\infty}{Pr} \qquad (z = \zeta_0), \tag{3.3a,b}$$

$$w_1 \to 0, \quad Dw_1 \to 0 \qquad (z \to \infty), \tag{3.3c,d}$$

where $D \equiv d/dz$. Equation (3.2) can be substantially simplified through the substitutions $s = e^{-(z-\zeta_0)/Pr}$ and $\alpha = kPr$, and by defining the small parameter
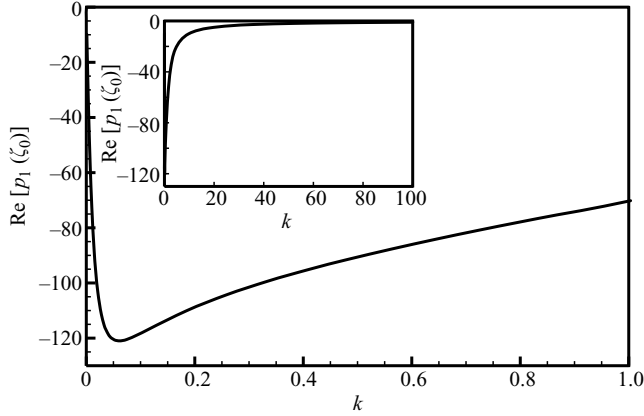
FIGURE 2. Real component of the pressure perturbation at the mush–liquid interface for $U_\infty = 100$ and $Pr = 10$. Note that the maximum pressure perturbation is $\mathrm{Re}[p_1(\zeta_0)] = -121$ at $k = 0.06$ which corresponds to a negative pressure perturbation at the peaks of the interfacial deflection. The inset graph shows the pressure perturbation over the range $k = [0, 100]$ as first reported in Neufeld *et al.* (2006).

$\epsilon = (i\alpha U_\infty)^{-1}$. The resultant equation and boundary conditions were solved by Neufeld *et al.* (2006) who found a Frobenius series solution of the form

$$w_1 = \lambda_1 s^{r_2} \sum_{j=0}^{\infty} a_j s^j + \lambda_2 s^{r_4} \sum_{j=0}^{\infty} b_j s^j. \qquad (3.4)$$

The negative roots of the indicial equation are given by

$$r_2 = -\alpha \quad \text{and} \quad r_4 = \frac{1}{2}[1 - \sqrt{1 + 4\alpha(\alpha + \epsilon^{-1})}], \qquad (3.5a, b)$$

and coefficients a_j and b_j are obtained from the general recurrence relation

$$\left[(j+r)^2 - \alpha^2\right]\left[(j+r)^2 - (j+r) - \alpha^2 - i\alpha U_\infty\right] a_j$$
$$= i\alpha U_\infty \left[\alpha^2 + 1 - (j+r-1)^2\right] a_{j-1}, \quad (3.6)$$

with $a_0 = 1$ and $b_0 = 1$. The constants λ_1 and λ_2 are given by

$$\lambda_1 = \frac{-i\alpha U_\infty/Pr}{\displaystyle\sum_{j=0}^{\infty}(r_2 + j)a_j - \beta \sum_{j=0}^{\infty}(r_4 + j)b_j} \quad \text{and} \quad \lambda_2 = -\beta\lambda_1, \qquad (3.7a, b)$$

where

$$\beta = \sum_{j=0}^{\infty} a_j \bigg/ \sum_{j=0}^{\infty} b_j. \qquad (3.8)$$

This solution of the perturbed velocities within the overlying liquid enables evaluation of the pressure perturbation felt at the mush–liquid interface, which is expressed by

$$p_1 = \frac{-\left(\mathrm{D}_s^2 - \alpha^2\right)\mathrm{D}s\,w_1 + \mathrm{D}_s^2 w_1}{\alpha^2}, \qquad (3.9)$$

where $\mathrm{D}_s \equiv s\,\mathrm{d}/\mathrm{d}s$. The pressure perturbation felt at the mush–liquid interface for an external flow of magnitude $U_\infty = 100$ is plotted in figure 2 as a function of the
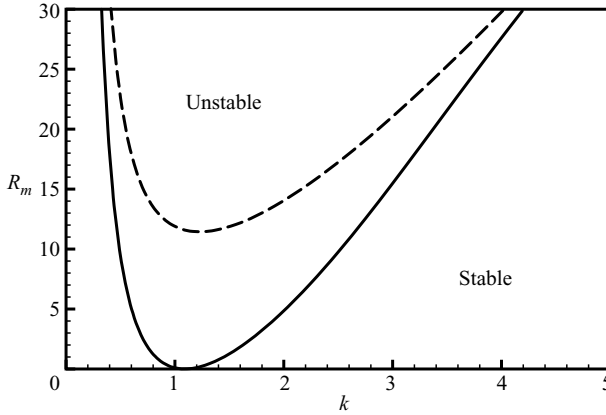
FIGURE 3. Neutral stability curves of the critical Rayleigh number as a function of wavenumber for $U_\infty = 0$ (dashed) and $U_\infty = 56\,748$ (solid) with parameters $Pr = 10$, $\Pi_0 = 10^{-5}$, $\mathscr{C} = 10.2$, $\mathscr{S} = 3.6$ and $\theta_\infty = 0.18$. Above the curves the system is unstable to convective motions while below the curves the system is stable.

wavenumber of the interfacial corrugation. We note that the pressure perturbation vanishes in the limit of an infinitely corrugated interface ($k \to \infty$) and in the limit of a planar interface ($k \to 0$) and is maximal for wavenumbers of order 0.1.

3.2. *Perturbed flow in the mushy layer*

The equations governing perturbations of heat, solid fraction and velocity within the mushy layer are

$$(D^2 + D - k^2)\theta_1 = \mathscr{S}D\phi_1 + w_1 D\theta_0, \tag{3.10}$$

$$(\mathscr{C} - \theta_0)D\phi_1 + (1 - \phi_0)D\theta_1 = \theta_1 D\phi_0 + \phi_1 D\theta_0 + w_1 D\theta_0, \tag{3.11}$$

$$(D^2 - k^2)w_1 = k^2 R_m \theta_1. \tag{3.12}$$

These perturbations are constrained by the following linearized boundary conditions. At the eutectic ($z = 0$) the temperature and velocity are

$$\theta_1 = 0 \quad \text{and} \quad w_1 = 0. \tag{3.13a,b}$$

The conditions on the mushy layer variables at the mush–liquid interface ($z = \zeta_0$) are

$$\theta_1 = -\zeta_1 \theta_\infty, \quad \phi_1 = \zeta_1 \theta_\infty / \mathscr{C}, \tag{3.14a,b}$$

$$D\theta_1 = \zeta_1 \Lambda \theta_\infty, \quad Dw_1 = -\zeta_1 \frac{k^2 \text{Re}[p_1(\zeta_0)]}{\Pi_0}, \tag{3.14c,d}$$

where $\text{Re}[p_1(\zeta_0)]$ is the real component of the pressure in the liquid at the mush–liquid interface.

This set of equations and associated boundary conditions form an eigenvalue problem that is solved numerically for eigenvalues (k, R_m, U_∞), the results of which are plotted in figure 3. This plot shows the curve of neutral stability for both a purely convective mode ($U_\infty = 0$), and a principally forced-convective mode ($U_\infty = 56748$), both for typical experimental values $\mathscr{C} = 10.2$, $\mathscr{S} = 3.6$ and $\theta_\infty = 0.18$. The stability of the forced-convective mode as a function of the external flow rate U_∞ can be readily characterized by the minimum, and therefore critical, Rayleigh number R_m^c as illustrated in figure 4. The plot, which demarcates regions that are stable to
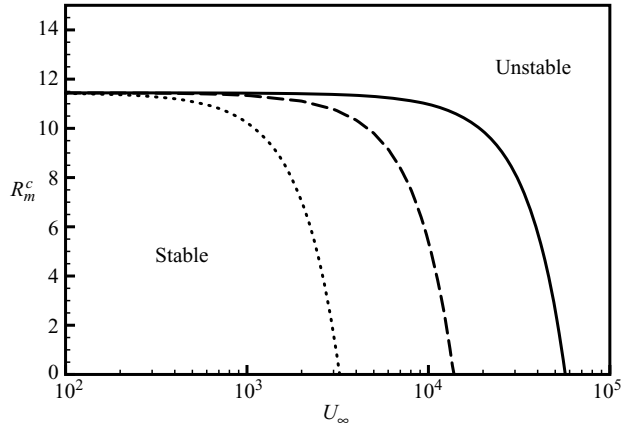
FIGURE 4. A plot of the critical porous-medium Rayleigh number as a function of the external flow rate for Darcy numbers $\Pi_0 = 10^{-3}$ (dotted), 10^{-4} (dashed) and 10^{-5} (solid). The average thermodynamic parameters of the experiments have been used: $\mathscr{C} = 10.2$, $\mathscr{S} = 3.6$ and $\theta_\infty = 0.18$.

convection from ones that are unstable, readily demonstrates the essential character of the instability. For small external shear rates a buoyant convective instability is dominant, and therefore the instability of the system is characterized well by a critical porous medium Rayleigh number. This buoyancy-driven convective mode is clearly identified with the mushy layer mode of convection first described by Worster (1992b). However, as the magnitude of the external shear flow is increased, the system is progressively destabilized by the external flow until at $U_\infty = U_\infty^c$ the critical Rayleigh number $R_m^c = 0$. For shear flows equal to, or in excess of, this critical magnitude, the fluid in the mushy layer is unstable to convective motions driven primarily by the externally imposed pressure perturbations at the mush–liquid interface. Because the mushy layer is a chemically reactive porous medium, fluid motion within its interstices is associated with alternating patterns of warming/cooling and solidification/dissolution as illustrated by the eigenfunctions plotted in figure 5. The pattern of solidification and dissolution shown in figure 5(b) is driven by the external flow and is most readily apparent at depth within the mushy layer. These patterns are typical of both the buoyant- and shear-driven mushy layer modes of convection and we have therefore interpreted the resultant patterns of solidification and dissolution in a similar manner to previous authors who focused only on the role of buoyant convection. This pattern of solidification and dissolution rapidly leads to the formation of crevasses which are elongated regions of zero solid fraction aligned perpendicular to the external flow as shown in §5.

3.3. *Experimental model and the role of permeability*

Figure 4 illustrates the central role that permeability plays in the forced mushy layer mode. While there currently exists a range of experimental results on the buoyant mushy layer mode in which $U_\infty = 0$ (for example Wettlaufer *et al.* 1997a in NaCl solution and Peppin *et al.* 2007 in aqueous NH$_4$Cl) our experimental investigations focus on the role of the forced mode of instability. Here we develop a semi-analytic theory in which buoyant convection is neglected ($R_m = 0$) and in which $\mathscr{C} \gg \theta_0$ as reflected in our experiments for which $\mathscr{C} \simeq 10$.
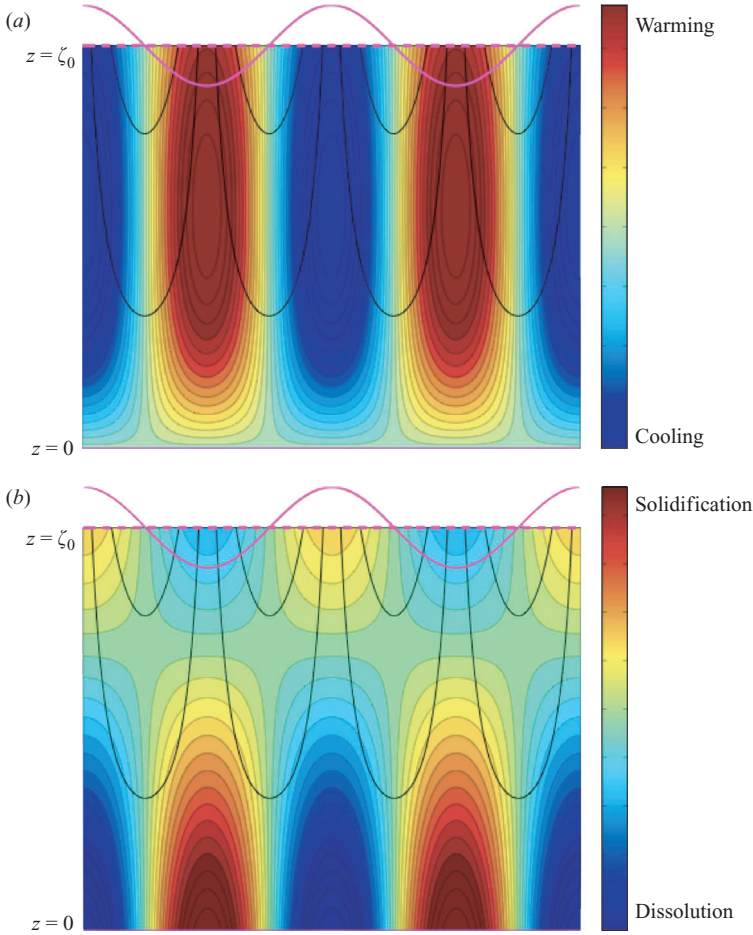
FIGURE 5. The results of the reduced model of mushy layer convection showing (*a*) perturbations to the thermal field and (*b*) perturbations to the solid fraction. Perturbations to the mush–liquid interface are shown in purple, and streamlines in black. Fluid motion, driven by pressure perturbations induced by the external flow, is upwards at the peaks and downwards at the troughs. Near the perturbed interface solidification at the peaks and dissolution at the troughs simply reflects the growth and recession of the perturbation. This restricted surface region has little effect on the overall pattern observed experimentally. The eigenfunctions plotted are for the experimental parameters $\mathscr{C} = 10.2$, $\mathscr{S} = 3.6$, $\theta_\infty = 0.18$, $Pr = 10$, $k = 1.09$, $R_m = 0$ and $U_\infty = 56\,748$.

In these limits, equations (3.10)–(3.12), which describe perturbations to the mushy layer, can be reduced to

$$(D^2 + \varLambda D - k^2)\theta_1 = w_1 \varLambda D\theta_0, \tag{3.15}$$

$$(D^2 - k^2)w_1 = 0. \tag{3.16}$$

Equation (3.16) together with boundary conditions (3.13*b*) and (3.14*d*) has a solution

$$w_1(z) = -\zeta_1 k \frac{\text{Re}[p_1(\zeta_0)]}{\Pi_0} \frac{\sinh(kz)}{\cosh(k\zeta_0)}. \tag{3.17}$$
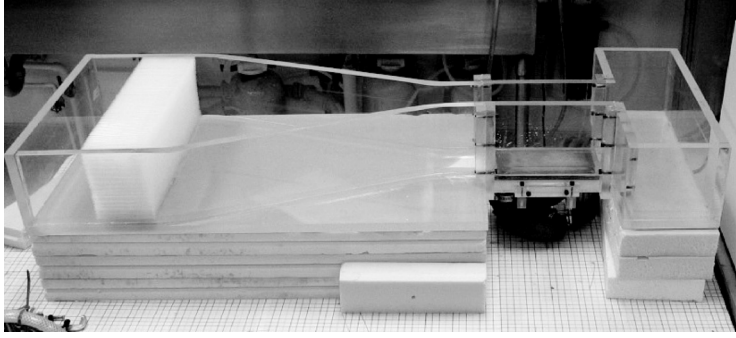
FIGURE 6. Image of the laboratory flume showing the entry sill on the left, straw baffle and confining walls which lead to the test section from which an NH_4Cl mushy layer is grown. Fluid is removed from the collection reservoir on the right and recirculated using corrosion-resistant pumps (not shown).

The thermal perturbations are solved using boundary conditions ($3.13a$) and ($3.14a$) giving

$$\theta_1(z) = \zeta_1 \theta_\infty \frac{\text{Re}[p_1(\zeta_0)]}{\Pi_0} \left\{ -e^{-\Lambda(z/2-\zeta_0)} \frac{\cosh(\gamma z)}{\cosh(k\zeta_0)} + e^{-\Lambda(z-\zeta_0)} \frac{\cosh(kz)}{\cosh(k\zeta_0)} \right.$$
$$\left. + e^{-\Lambda(z-\zeta_0)/2} \frac{\sinh(\gamma z)}{\sinh(\gamma\zeta_0)} \left[e^{\Lambda\zeta_0/2} \frac{\cosh(\gamma\zeta_0)}{\cosh(k\zeta_0)} - 1 \right] \right\}$$
$$- \zeta_1 \theta_\infty e^{-\Lambda(z-\zeta_0)/2} \frac{\sinh(\gamma z)}{\sinh(\gamma\zeta_0)} \tag{3.18}$$

where $\gamma = \sqrt{\Lambda^2 + 4k^2}/2$. Finally, we impose conservation of heat at the mush–liquid interface through the Stefan condition ($3.14c$). This provides a dispersion relation for the permeability of the mushy layer necessary for flow forced by the motion of the external fluid;

$$\Pi_0(k) = \text{Re}[p_1(\zeta_0)] \left\{ \frac{\gamma e^{\Lambda\zeta_0/2}}{\cosh(k\zeta_0)} \left[\frac{\cosh(\gamma\zeta_0)}{\tanh(\gamma\zeta_0)} - \sinh(\gamma\zeta_0) \right] \right.$$
$$\left. + k \tanh(k\zeta_0) - \frac{\Lambda}{2} - \frac{\gamma}{\tanh(\gamma\zeta_0)} \right\} \left\{ \frac{\Lambda}{2} + \frac{\gamma}{\tanh(\gamma\zeta_0)} \right\}^{-1}. \tag{3.19}$$

Using this result we find the minimum critical Darcy number as a function of the external flow speed

$$\Pi_0^c = a \left(U_\infty^c \right)^b, \tag{3.20}$$

where $a = 409.20$ and $b = -1.60$ are obtained from a numerical fit of the critical permeability derived from (3.19). This power-law dependence of the critical permeability on the magnitude of the external flow rate is verified by the experimental results of §5 and, importantly, results in an estimation of the dimensional permeability of the NH_4Cl mushy layer.

4. Experimental apparatus and methods

The experimental apparatus shown in figure 6 is designed for controlled growth of an NH_4Cl mushy layer in the presence of a laminar flow of prescribed far-field velocity. The apparatus consists of a large Perspex laboratory flume 1.6 m in
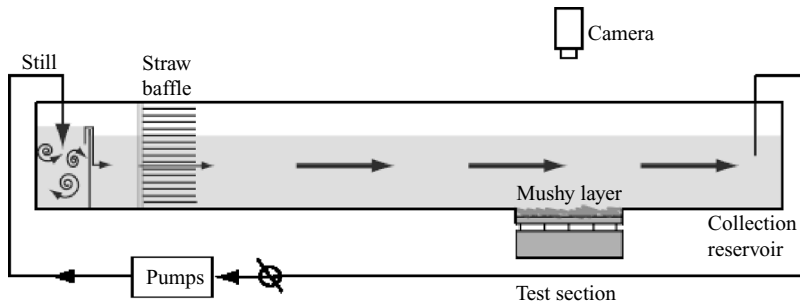
FIGURE 7. Schematic of the laboratory flume. Pumps recirculate the working fluid into an initial reservoir. The fluid flows over a sill, through a straw baffle and a narrowing section to produce an ideal, laminar profile before transiting over the test section. Finally the fluid is pumped out to the collection reservoir. Flow control is achieved through the use of a recirculation line with associated valves.

length with a depth of 15 cm. As illustrated in figure 7, flow is generated within the flume by two corrosion-resistant pumps that inject the NH_4Cl solution behind a sill thereby dampening the initial turbulent discharge. The solution then passes through a baffle and a pair of constricting walls that produce a laminar flow field at the experimental velocities considered. The confining walls are constructed from two custom moulded Perspex walls whose angle with respect to the flow direction was chosen to eliminate vortex generation at the sidewalls. This laminar flow then passes over a test section where an NH_4Cl mushy layer is grown at constant rate from a base plate whose temperature can be varied as a function of time (as detailed in the following subsections). Ultimately, the solution enters the collection reservoir and is recirculated.

Using this apparatus a typical experimental run proceeds as follows. An NH_4Cl mushy layer is grown at constant rate from a cooled plate recessed 5 mm from the base of the quiescent flume ($U_\infty = 0$). Once the free surface of the mushy layer is at the same height as the base of the flume the external flow is initiated ($U_\infty > 0$) thus ensuring that the viscous boundary layer remains uniform as it transitions from flow over the Perspex flume to that over the mushy layer. Typical growth rates of the mushy layer are 10^{-4}–10^{-3} cm s^{-1} which therefore have a negligible impact on the bulk flow on the time scales over which the forced instability develops. Secondly, and perhaps most importantly, by performing a series of experiments in which both the thermal forcing and experimental parameters were unchanged, but in which no external flow was applied, we observed evidence of the mushy layer mode of convection only after a depth of 8–10 mm was reached. Thus, once the external flow has been initiated any morphological change in the mushy layer can be directly attributed to forcing by the external flow.

4.1. *Thermal control of mushy layer growth*

4.1.1. *A model for thermal control*

Steady-state growth of the mushy layer is achieved through temporal control of the temperature at the base of the test section. A model prescribing the required thermal forcing has been developed and is based on the steady-state solutions derived in § 2. To first approximation, solidification occurs at the base plate once the temperature reaches the liquidus temperature at bulk concentration. The temperature required at
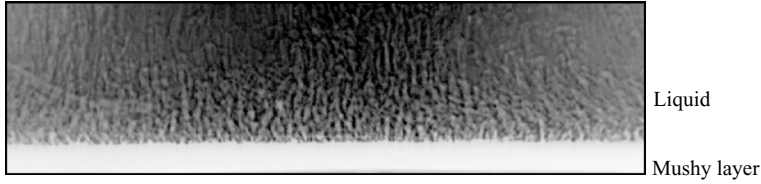
Liquid

Mushy layer

FIGURE 8. Vigorous, small-scale, compositional convection in the fluid ahead of the mushy layer in the absence of external flow as seen from the side in this negative shadowgraph image of a growing mushy layer. The boundary layer mode of convection does not have a significant effect on the mushy layer morphology implying that the mushy layer remains unperturbed despite vigorous convection above it. The depth of the mushy layer shown is 2 mm.

the base plate $T_b(t)$ is therefore given by

$$T_b(t) = T_L(C_0) + \frac{T_\infty - T_L(C_0)}{\Lambda} \left[1 - \exp(\Lambda V^2 t/\kappa)\right], \qquad (4.1)$$

through a coordinate transformation of the steady-state thermal solution (2.15) to a reference frame fixed at the copper base plate.

4.1.2. *The effect of convection in the liquid*

Typical experiments on the growth of NH_4Cl mushy layers in the absence of externally imposed flows show that the system is unstable to the boundary layer mode well in advance of the mushy layer mode. The onset of this mode results in vigorous, small-scale fluid motion in the compositional boundary layer ahead of the mush–liquid interface while leaving the fluid within the mushy layer effectively stagnant as shown in figure 8. This rapid convection drives both thermal and compositional fluxes exceeding those predicted by diffusion alone. We therefore use the approach of Worster & Kerr (1994) in modifying the thermal flux in the liquid at the mush–liquid interface by a convective flux F_T. Thus, the Stefan condition becomes

$$\left.\frac{\partial \theta}{\partial z}\right|_{z=\zeta_0} = \frac{F_T}{cV\Delta T}, \qquad (4.2)$$

where c is the specific heat defined below. Convection within the boundary layer is driven primarily by the compositional perturbations. Therefore, compositional Nusselt and Rayleigh numbers are defined as

$$Nu_C = \frac{F_C}{D(C_0 - C_i)/d} \quad \text{and} \quad R_C = \frac{g\tilde{\beta}(C_0 - C_i)d^3}{D\nu}$$

respectively, where d is the depth of the compositional boundary layer, F_C is the compositional flux and D is the solutal diffusivity. By making the standard assumption that the compositional flux is independent of the boundary layer thickness the four-thirds law is recovered,

$$F_C = 2^{4/3}\lambda D \left(\frac{g\tilde{\beta}}{D\nu}\right)^{1/3} (C_0 - C_i)^{4/3}, \qquad (4.3)$$

where λ is a constant. Finally, it is assumed that this compositional flux drives a thermal flux given by the relation

$$F_T = A\frac{k}{D}\left(\frac{T_\infty - T_i}{C_0 - C_i}\right)F_C$$

$$= 2^{4/3}\lambda Ak\left(\frac{g\tilde{\beta}}{D\nu}\right)^{1/3}(T_\infty - T_i)(C_0 - C_i)^{1/3}, \qquad (4.4)$$

Parameter	Symbol	Value	Reference
eutectic concentration	C_E	19.7 wt%	Washburn (2003)
eutectic temperature	T_E	$-15.4\,°C$	Washburn (2003)
liquidus slope (super-eutectic)	Γ	$4.72 \pm 0.07\,\mathrm{K\,wt\%}^{-1}$	Washburn (2003)
kinematic viscosity	ν	$9.54 \times 10^{-3}\,\mathrm{cm^2\,s^{-1}}$	Sarazin & Hellawell (1988)
latent heat	$\mathscr{L}$	$421.95\,\mathrm{J\,cm^{-3}}$	Worster & Kerr (1994)
thermal expansion coefficient	$\tilde{\alpha}$	$6 \times 10^{-4}\,\mathrm{K^{-1}}$	Sarazin & Hellawell (1988)
solutal expansion coefficient	$\tilde{\beta}$	$2.5 \times 10^{-3}\,\mathrm{wt\%}^{-1}$	Worster & Kerr (1994)
solute diffusivity	D	$1.3 \times 10^{-5}\,\mathrm{cm^2\,s^{-1}}$	Sarazin & Hellawell (1988)
specific heat of solid	c_s	$0.545\,\mathrm{cal\,cm^{-3}\,K^{-1}}$	Worster & Kerr (1994)
specific heat of solution	c_l	$0.847\,\mathrm{cal\,cm^{-3}\,K^{-1}}$	Worster & Kerr (1994)
thermal conductivity of crystal	k_s	$5.26 \times 10^{-3}\,\mathrm{cal\,cm^{-1}\,s^{-1}\,K^{-1}}$	Worster & Kerr (1994)
thermal conductivity of liquid	k_l	$1.39 \times 10^{-3}\,\mathrm{cal\,cm^{-1}\,s^{-1}\,K^{-1}}$	Worster & Kerr (1994)
inter-dendrite spacing	$\delta_{dendrite}$	0.03 cm	Worster (2000)
kinetic growth parameter	$\mathscr{G}$	$4.14 \times 10^{-5}\,\mathrm{cm\,s^{-1}\,K^{-2}}$	Worster & Kerr (1994)

TABLE 1. Physical properties of aqueous ammonium chloride solution and its crystalline solid phase.

where A is a constant which depends on the ratio of thermal to compositional diffusivities. Worster & Kerr (1994) note that the parameter A is about unity for the weak double-diffusive form of convection typical within the compositional boundary layer and thus we set $A = 1$.

4.1.3. *Kinetic undercooling*

The model of mushy layer growth can be further expanded by relaxing the assumption that the temperature and concentration within the mushy layer are constrained by the liquidus relationship. Specifically, recognizing that solidification is an intrinsically non-equilibrium process a model of kinetic undercooling is introduced. Following Worster & Kerr (1994), this undercooling is parameterized as

$$\frac{\partial \zeta}{\partial t} = V = \mathscr{G}[T_L(C_0) - T_i]^2, \tag{4.5}$$

where $\mathscr{G} = 4.14 \times 10^{-5}\,\mathrm{cm\,s^{-1}\,°C^{-2}}$ is a so-called kinetic growth parameter. Rearranging this expression for the interfacial temperature gives

$$T_i = T_L(C_0) - \sqrt{V/\mathscr{G}},$$

and therefore the full equation describing the base-plate temperature required for constant growth of a mushy layer is given by

$$T_b(t) = T_L(C_0) - \sqrt{V/\mathscr{G}} + \frac{F_T}{\Lambda cV}\left[1 - \exp\left(\Lambda \frac{V^2}{\kappa}t\right)\right], \tag{4.6}$$

where F_T is defined by (4.4). The parameter values, $A = 1$ and $\lambda = 0.0101$, used for the experiment are taken from Worster & Kerr (1994) who also studied the NH$_4$Cl mushy layer system. All other constants are given in table 1. Furthermore, 'ideal' mushy layer theory neglects variations in the physical properties of the liquid and solid phases. To first approximation, the thermal conductivity k and specific heat c of the mushy layer are estimated as $k = \phi k_s + (1 - \phi)k_l$ and $c = \phi c_s + (1 - \phi)c_l$, where k_s, k_l, c_s and c_l are the thermal diffusivities and specific heats of the solid and liquid respectively (listed in table 1). A depth-averaged value of $\phi = 0.6$ has been taken

from the post-growth CT scan measurements of the solid fraction of a similar NH_4Cl mushy layer described by Chen *et al.* (1994).

4.2. *Experimental realization and measurement of constant growth*

Controlled solidification of an NH_4Cl mushy layer is accomplished in the following manner. The base of the test section is recessed 5 mm from the base of the flume and is composed of a 2 mm thick copper plate whose temperature is monitored and controlled by a computer running Labview. The temperature at the base of the mushy layer is monitored by three thermocouples embedded within the copper base plate. This provides the necessary input for control, which is achieved by two elements. The first is an array of Peltier devices, or thermoelectric coolers, which are held in thermal contact with the copper base plate. These Peltier devices produce a thermal flux proportional to the applied electrical power, and thus provide a mechanism for relatively fast thermal control of the base plate. The flux through the array of Peltier devices is controlled by a power supply that is manipulated by the Labview program. Underlying this array is a brass manifold through which 14 l of coolant is circulated by two RTE-7 Neslab baths. In practice, owing to the large thermal inertia associated with the large volume of coolant, these Neslab baths provide temperature control and stability over long time scales while the Peltier devices provide accurate, and enhanced, temperature control on shorter time scales. In this way, a prescribed temporal variation of the temperature of the base plate can be used to force steady-state growth of the overlying mushy layer.

The experiment is visualized in two ways. At regular intervals shadowgraph images of the side of the test section are taken. From these images the depth of the mushy layer is calculated as a function of time. A second set of images is taken of the planform of the resultant mushy layer. It is through examination of these images that the presence of the forced mushy layer mode is detected.

Measurements of the thermal variables, the power applied to the Peltier array, and the resultant evolution of the height of the mushy layer from a typical experimental run are shown in figure 9(*a–c*). In figure 9(*b*) the theoretical model governing the steady-state growth of an NH_4Cl mushy layer is shown along with the experimentally achieved thermal forcing. It is apparent that, after an initial thermal transient, the base-plate temperature achieved was in good agreement with the model forcing until 800 s into the experiment. This is ensured through gradual cooling of the manifold by the Neslab baths, and through rapid application of electric power (shown in figure 9*c*) to the Peltier devices. It should also be noted that, as shown by the dotted line in figure 9(*b*), owing to the large fluid volume contained within the laboratory flume, the far-field temperature did not vary appreciably during the course of the experiment. The resultant mushy layer growth is shown in figure 9(*a*). Here, after an initial transient, linear growth of the mushy layer is achieved. At $t = 420$ s, shown in figure 9(*a*) by the vertical grey bar, an external flow was initiated of $\tilde{U}_\infty = 8.4$ cm s^{-1}. This produces an initial transient in mushy layer growth, most probably associated with patterns of solidification and dissolution driven by the external flow. The solidification then continues with a lower growth rate most probably due to a greater volume-averaged solid fraction. This is consistent with the solidification/dissolution patterns considered in §3 and described in §5 and mirrors the increased solid fraction observed when fluid motion is driven by interstitial buoyancy as measured *in situ* through MRI imaging by Aussillous *et al.* (2006).
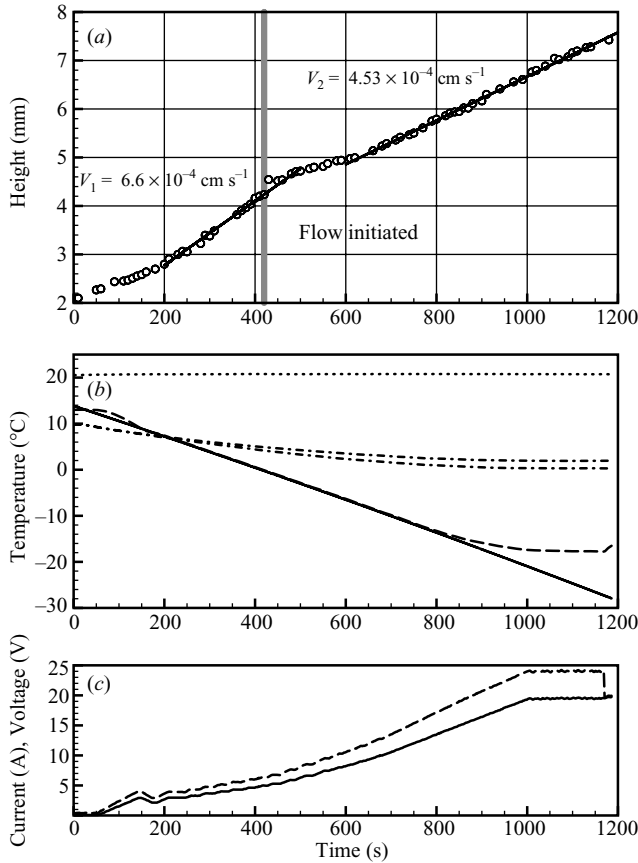
FIGURE 9. Typical thermal forcing and response from experiment 250106C (see table 2). (*a*) The height of the mushy layer as a function of time (○) and the best-fit line (solid) of the growth velocity measured both before and after application of the external flow (indicated by grey shading). (*b*) The temperature forcing required for constant growth (solid) and the achieved base place temperature (dashed) along with the bulk fluid temperature (dotted), and the temperature of the two Neslab cooling baths (dash–dot). (*c*) The current (solid) and the voltage (dashed), and hence the power, applied to the base plate to achieve the required forcing. See text for further details.

5. Experimental results and discussion

The experimental apparatus and methods described in §4 have been used to perform a systematic study of the effects of an applied external flow on the development of a mushy layer grown at constant rate. Owing to the breadth of parameter space, and the constraints imposed by selection of NH_4Cl as the working solution we focus our attention on variations in the magnitude of the external shear (U_∞) only, keeping the thermodynamic parameters $\mathscr{C}$, $\mathscr{S}$ and θ_∞ relatively constant. Experimentally this is achieved through variation of the dimensional growth velocity V through thermal forcing of the base plate, and variation of the dimensional magnitude of the external flow $\tilde{U}_\infty$. A summary of the experimental conditions, along with the measured values of the thermodynamic parameters is presented in table 2.

Each experiment begins with the linear growth of an NH_4Cl mushy layer within the quiescent laboratory flume as described in §4. The typical planform of the mushy layer just prior to the initiation of an external flow is shown in figure 10(*a*). In all

Designation	$\tilde{U}_\infty$ (cm s^{-1})	$V(\times 10^{-4}$ cm s^{-1})	$U_\infty(\times 10^3)$	$\mathscr{C}$	$\mathscr{S}$	θ_∞	stable/ unstable
071105A	4.9 ± 0.1	9.4 ± 0.3	5.2 ± 0.1	10.86	3.86	0.18	stable
071105B	12 ± 1	7 ± 1	17 ± 0.3	10.86	3.86	0.17	unstable
071105C	8.2 ± 0.4	7.41 ± 0.07	11.1 ± 0.06	10.86	3.86	0.16	unstable
071105D	5.8 ± 0.2	7.6 ± 0.1	7.7 ± 0.3	10.86	3.86	0.29	unstable
071105E	2.99 ± 0.07	8.00 ± 0.09	3.74 ± 0.09	10.86	3.86	0.30	stable
161105A	12 ± 1	8.2 ± 0.1	15 ± 0.2	9.93	3.56	0.12	unstable
161105B	8.4 ± 0.4	6.57 ± 0.09	12.7 ± 0.06	9.93	3.56	0.12	unstable
161105C	4.7 ± 0.1	7.4 ± 0.1	6.3 ± 0.1	9.93	3.56	0.15	stable
220106A	10 ± 1	8 ± 1	12 ± 0.2	10.47	3.73	0.23	unstable
220106B	10 ± 1	9.5 ± 0.1	10 ± 0.1	10.47	3.73	0.23	unstable
230106A	9 ± 1	10.8 ± 0.04	8 ± 1	10.81	3.84	0.30	unstable
230106B	9 ± 1	8.9 ± 0.1	10 ± 1	10.47	3.73	0.27	unstable
230106C	9 ± 1	9.3 ± 0.1	9 ± 1	10.47	3.73	0.25	unstable
230106D	9 ± 1	3.19 ± 0.02	27 ± 0.3	10.47	3.73	0.24	unstable
230106E	5.8 ± 0.2	10.5 ± 0.04	5.5 ± 0.3	10.47	3.73	0.27	unstable
250106C	8.4 ± 0.4	6.6 ± 0.1	12.7 ± 0.07	10.31	3.68	0.08	unstable
250106D	3.60 ± 0.08	5.72 ± 0.06	6.3 ± 0.1	10.31	3.68	0.20	stable
250106E	3.60 ± 0.08	9.7 ± 0.1	3.72 ± 0.09	10.31	3.68	0.19	stable
250106F	3.60 ± 0.08	9.8 ± 0.2	3.68 ± 0.08	10.31	3.68	0.19	stable
280106A	4.7 ± 0.1	3.93 ± 0.06	11.9 ± 0.03	9.85	3.53	0.13	stable
280106B	4.7 ± 0.1	5.1 ± 0.1	9.2 ± 0.2	9.85	3.53	0.12	stable
280106C	4.7 ± 0.1	2.11 ± 0.01	22.2 ± 0.05	9.85	3.53	0.12	stable
280106D	4.7 ± 0.1	8.6 ± 0.2	5.4 ± 0.1	9.85	3.53	0.12	stable
300106A	8.6 ± 0.6	3.94 ± 0.03	22 ± 0.2	10.00	3.58	0.15	unstable
300106B	8.6 ± 0.6	4.55 ± 0.04	19 ± 0.1	10.00	3.58	0.04	unstable
300106C	8.6 ± 0.6	2.280 ± 0.009	38 ± 0.3	10.00	3.58	0.19	unstable
300106D	3.86 ± 0.09	7.58 ± 0.07	5.1 ± 0.1	10.00	3.58	0.18	stable

TABLE 2. Summary of experiments in which a shear flow was applied. Growth velocities were measured prior to the application of the external flow. The presence of the channel pattern upon application of an external flow of velocity U_∞ is indicated by stable/unstable and results in the channelling pattern typified by the results shown in figure 10(b).

experiments, the planform reveals a homogeneous mushy layer; evidence that the mushy layer mode of convection is absent prior to initiation of the shear flow. Any changes in the morphology of the mushy layer upon application of the external flow are recorded and can be systematically correlated with the strength of the external current. For sufficiently weak shear flows growth of the mushy layer remains unaffected and the observed planform remains homogeneous. These experiments in which the mushy layer is homogeneous in the presence of flow are denoted 'stable' in table 2. In contrast, application of an external flow of sufficient magnitude results in a dramatic series of dark striations that form perpendicular to the applied flow, as shown in figure 10(b). These striations are regions of zero solid fraction, or crevasses, through which the black base plate can be clearly seen. Regions of zero solid fraction within the mushy layer reveal the influence of flow leading to dissolution and solidification through advection of heat and solute. The presence of these crevasses, whose spacing is commensurate with the depth of the mushy layer, is consistent with the patterns of dissolution and solidification produced by forced convective rolls aligned perpendicular to the applied flow. We therefore interpret these crevasses as the nonlinear manifestation of the forced mushy layer mode of convection. Experiments in which this pattern of crevasses are clearly visible are denoted 'unstable' in table 2.
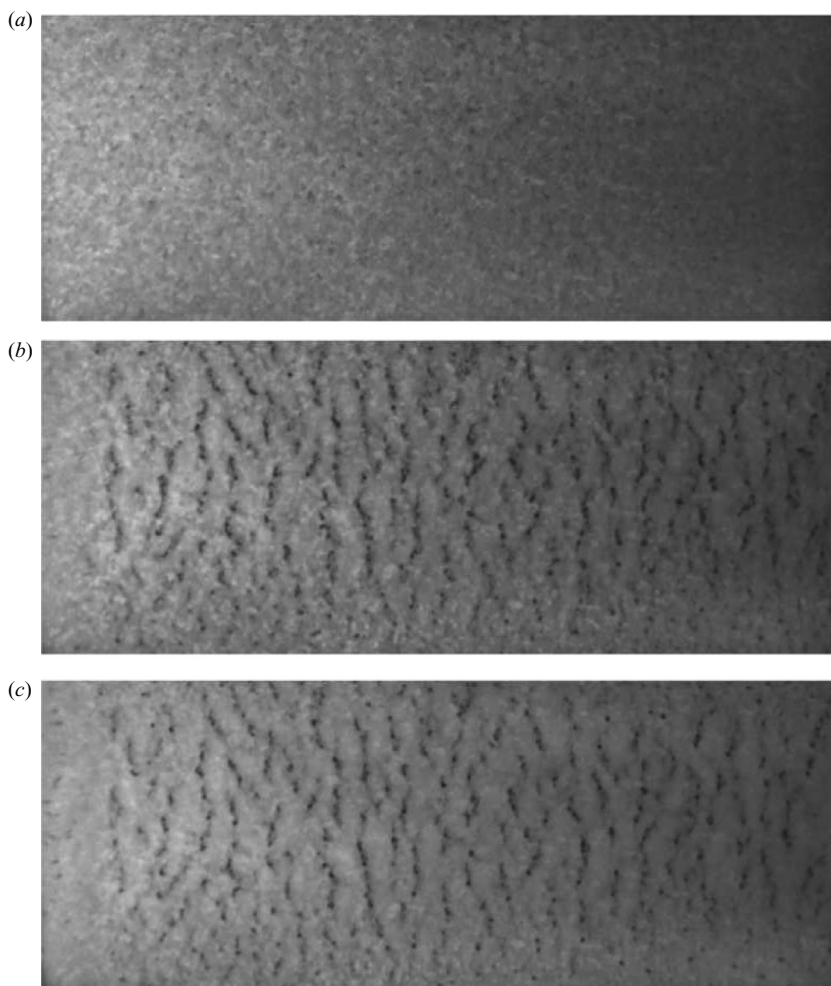
FIGURE 10. Images from experiment 300106B (see table 2) showing a planform view of the mushy layer (*a*) prior to onset, (*b*) after an external flow of $\tilde{U}_\infty = 8.6$ cm s^{-1} has been applied from left to right in the photos and (*c*) several minutes after the flow has been applied. Note that the dark patterns are regions of zero solid fraction through which the black base plate can be seen.

The subsequent evolution of these crevasses in the continued presence of the external shear flow is typified by the planform shown in figure 10(*c*). This image shows the breakdown of the crevasses into a series of point regions of zero solid fraction referred to as chimneys in §1. Continued growth of the mushy layer results in a decrease in the number density of these chimneys, a result first observed in the absence of an external flow by Tait & Jaupart (1992) and Huppert *et al.* (1993). Finally, we note that the formation of the pattern of crevasses is re-entrant; that is, once the external flow has ceased, the mushy layer returns to the homogeneous state through further crystal growth.

A quantitative comparison between the experimental results and the stability analysis of §3 is made in the following manner. The simplified theoretical analysis outlined in §3, and presented in more detail by Neufeld & Wattlaufer (2008), shows

Parameter	Symbol	Value
concentration ratio	$\mathscr{C}$	10.2 ± 0.3
Stefan number	$\mathscr{S}$	3.6 ± 0.1
superheat	θ_∞	0.18 ± 0.07
Prandtl number	Pr	10

TABLE 3. Average non-dimensional parameters used in the theoretical comparison with the suite of experiments listed in table 2. Errors quoted are ± 1 standard deviation.
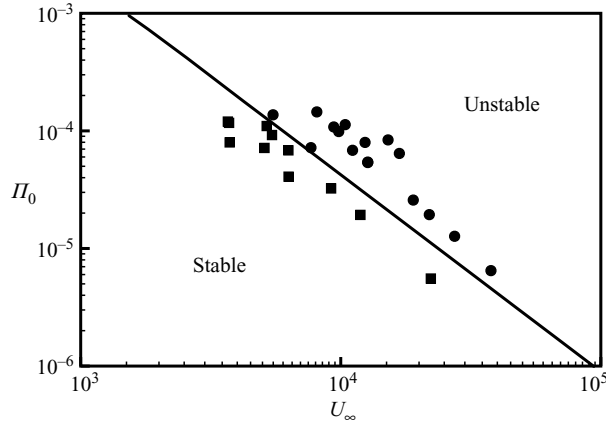

FIGURE 11. Comparison of theoretical prediction of the stability threshold given by (3.20) with the experimental results. Squares indicate experiments in which the externally applied shear flow had no discernible effect on the mushy layer and circles indicate experiments in which corrugations became apparent upon application of the external flow. A value for the dimensional permeability $\tilde{\Pi}_0 = 1.75 \times 10^{-3}$ cm^2 was used. See text for details.

that the dominant parameter controlling the interaction of an external flow with solidification of a mushy layer is the permeability of the crystal matrix. The key result of the linear stability analysis presented in §3 is therefore the power-law relationship (3.20) between the magnitude of the critical external flow U_∞^c and the permeability of the mushy layer, as characterized by the Darcy number Π_0. This relationship separates regions that are stable to the forced convective mode from ones that are unstable and therefore prone to development of crevasses. The experimental observations of the absence/presence of crevasses, as indicated in table 2 by stable/unstable, are compared to this theoretical prediction in the following manner. We first note that there are no adjustable parameters in the power-law relationship. However, in constructing the dimensionless groups characterizing the experiments we note that while the growth rate V and dimensional external flow rate $\tilde{U}_\infty$ are experimentally well constrained, previous estimates of the dimensional permeability $\tilde{\Pi}_0$ vary by orders of magnitude within the literature. Because each experiment has been conducted using fixed thermodynamic parameters, $\mathscr{C}$, $\mathscr{S}$ and θ_∞ (summarized in table 3) we anticipate that a single dimensional permeability characterizes the entire suite of 27 experiments. Using this dimensional permeability as a fitting parameter we find good agreement between our linear stability analysis and the experimental data as shown in figure 11. Here the matching power-law behaviour gives us confidence in our analysis, and confirms the central role of the external shear U_∞ and permeability Π_0 in the

forced instability and the relative insensitivity to the porous Rayleigh number R_m as predicted in figure 4. Finally, a comparison of the magnitudes represents the following fit of the dimensional mushy layer permeability:

$$\tilde{\Pi}_0 = 1.75 \times 10^{-3} \text{ cm}^2. \tag{5.1}$$

This estimate compares quite favourably with a theoretical estimate obtained in the following manner. We estimate the depth-averaged solid fraction by integration of the steady-state solid fraction profile over the depth of the mushy layer. For the typical experimental parameters $\mathscr{C} = 10.2$, $\mathscr{S} = 3.6$ and $\theta_\infty = 0.18$ we find

$$\begin{aligned}
\overline{\phi}_0 &= \frac{1}{\zeta_0} \int_0^{\zeta_0} \phi_0 \, \mathrm{d}z \\
&= \frac{\theta_\infty}{\Lambda \mathscr{C}} \left[\frac{1}{\zeta_0 \theta_\infty} - 1 \right] \\
&\simeq 0.03.
\end{aligned} \tag{5.2}$$

We estimate the permeability of the mushy layer using the Kozeny–Carman relation and an inter-dendrite spacing between $\delta_{dendrite} \simeq 0.03$ and 0.05 cm given by Worster (2000) and Chen & Chen (1991) respectively. This yields a theoretical estimate of the mushy layer permeability of

$$\tilde{\Pi}_{0,theory} = 4.2 - 11.7 \times 10^{-3} \text{ cm}^2, \tag{5.3}$$

in good agreement with the experimentally determined value. We note that these estimates of NH_4Cl mushy layer permeability are much larger than the estimates of previous authors. In particular, we note that the estimate given by Chen & Chen (1991) of $\tilde{\Pi}_0 = 2.41 \times 10^{-5}$ cm^2 is based on measurements of the solid fraction obtained by CT scans of an NH_4Cl mushy layer two days after the experiments exhibiting the fully developed mushy layer mode, including the presence of chimneys, were conducted. First, their estimate of the permeability was derived using the Kozeny–Carman relationship, with a typical dendrite spacing of $\delta_{dendrite} = 0.05$ cm. Secondly, the more recent *in-situ* MRI measurements of sucrose mushy layers conducted by Aussillous *et al.* (2006) indicate that the mushy layer mode of convection tends to increase the depth-averaged solid fraction of the mushy layer. It is therefore not surprising that our results indicate a higher mushy layer permeability. Our experimentally determined value of the permeability of an NH_4Cl mushy layer therefore presents a relatively rare dynamical estimate of this important parameter. It is more commonly the case that such quantities are measured without reference to a critical condition such as this, where the system is operating near a stability threshold.

This dynamical approach has been successful in characterizing the onset of the mushy layer mode (see Wettlaufer *et al.* 1997*a*, *b*) and we hope that it can provide a context for further studies of the forced mode. In analogy with the work of Wettlaufer *et al.* (1997*a*) figure 11 can therefore be considered as an empirical marginal stability diagram separating regimes that are unstable to the forced mushy layer mode from those that are stable. In the case of forced convection the reduced analytic model indicates the existence of a scaling relationship between the external flow velocity U_∞ and the Darcy number Π_0. Figure 11 therefore not only supports the scaling relationship, and hence the underlying theory, but as a result provides a measure of the underlying dimensional permeability. This last result is of great importance because flow within a mushy layer is dominated by the permeability of the matrix. Therefore, the resulting comparison between theory and experiment has implications

not only for problems of externally forced flows in mushy layers, but to any problem in which flow within the mushy layer plays an important role.

6. Conclusion

The interaction of an external flow with the solidification of a growing mushy layer has been investigated both theoretically and experimentally. The full numerical linear stability analysis of Neufeld & Wettlaufer (2008), and the reduced model presented here, reveal that the presence of a sufficiently vigorous external shear can force flow within the mushy layer in the form of rolls aligned perpendicular to the external shear. The linear stability analysis further predicts that this motion will lead to patterns of solidification and dissolution caused by, and transverse to, this forced flow.

These theoretical predictions were tested using an aqueous ammonium chloride solution which was solidified at constant rate within a laboratory flume. We observe the formation of a striking pattern of crevasses, regions of zero solid fraction, aligned perpendicular to the external shear. The presence/absence of these crevasses was compared with the linear stability analysis and in so doing a highly constrained dynamical estimate of the permeability of the mushy layer was obtained.

This combination of theoretical and experimental approaches reveals that the interaction of an external flow with the growth of a dendritic array of crystals can lead to dramatic changes in the morphology of the resultant solid. Furthermore, we have shown the central role that the permeability of the mushy layer plays in the forced convective instability. The physical mechanisms demonstrated here may therefore be important to a host of geophysical and industrial systems. For example, measurements of the speed of tidal currents performed by Widell, Fer & Haugan (2006) have been correlated with salt fluxes from warm, and therefore permeable, sea ice. These oceanic flows may therefore alter the nature of heat and salt fluxes from sea ice thereby changing both the properties of the overlying ice as well as the hydrography of the polar oceans. The feedback may continue to influence the system by modification of the mechanical properties, such as bending rigidity, and hence the deformation patterns of the ice cover (Vella & Wettlaufer 2007). Our results also suggest that the presence of an external flow could enhance the colonization of sea ice because the decreased solid fraction provides both the nutrients and habitat necessary for polar organisms. Such an idea has been investigated more qualitatively by Krembs, Tuschling & von Juterzenka (2002) in which flow over a prescribed bottom topography was found to affect the spatial distribution of the colonization of sea ice. In industrial applications the suite of experiments reported on here demonstrates the possibility of tailoring materials using external flows. Moreover, the role of such flows on the solidification textures of the Earth's inner core is thought to be related to its elastic anisotropy (Aubert *et al.* 2008) although the issue is not without continuing and exciting controversy (Belonoshko *et al.* 2008). Thus, the theoretical treatment and experimental methods outlined here therefore provide a guide for future studies on the interaction of external flows with a wide range of systems.

REFERENCES

Aubert, J., Amit, H., Hulot, G. & Olson, P. 2008 Thermochemical flows couple the Earth's inner core growth to mantle heterogeneity. *Nature* **454**, 758–761.

Aussillous, P., Sederman, A. J., Gladden, L. F., Huppert, H. E. & Worster, M. G. 2006 Magnetic resonance imaging of structure and convection in solidifying mushy layers. *J. Fluid Mech.* **552**, 99–125.

BEAVERS, G. S. & JOSEPH, D. D. 1967 Boundary conditions at a naturally permeable wall. *J. Fluid Mech.* **30**, 197–207.

BELONOSHKO, A. B., SKORODUMOVA, N. V., ROSENGREN, A. & JOHANSSON, B. 2008 Elastic anisotropy of Earth's inner core. *Science* **319**, 797–800.

CHEN, C. F. & CHEN, F. 1991 Experimental study of directional solidification of aqueous ammonium chloride solution. *J. Fluid Mech.* **227**, 567–586.

CHEN, F., LU, J. W. & YANG, T. L. 1994 Conective instability in ammonium chloride solution directionally solidified from below. *J. Fluid Mech.* **276**, 163–187.

CHUNG, C. A. & CHEN, F. 2001 Morphological instability in a directionally solidifying binary solution with an imposed shear flow. *J. Fluid Mech.* **436**, 85–106.

COPLEY, S. M., GIAMEI, A. F., JOHNSON, S. M. & HORNBECKER, M. F. 1970 The origin of freckles in binary alloys. *Metall. Trans.* **1**, 2193–2204.

DAVIS, S. H. 1990 Hydrodynamic interactions in directional solidification. *J. Fluid Mech.* **212**, 241–262.

DAVIS, S. H. 2001 *Theory of Solidification*. Cambridge University Press.

FELTHAM, D. L. & WORSTER, M. G. 1999 Flow-induced morphological instability of a mushy layer. *J. Fluid Mech.* **391**, 337–357.

GLICKSMAN, M. E., CORIELL, S. R. & MCFADDEN, G. B. 1986 Interaction of flows with the crystal-melt interface. *Annu. Rev. Fluid Mech.* **18**, 307–335.

HUPPERT, H. E., HALLWORTH, M. A. & LIPSON S. G. 1993 Solidification of NH_4Cl and NH_4Br from aqueous solutions contaminated by $CuSO_4$: the extinction of chimneys. *J. Cryst. Growth* **130**, 495–506.

KREMBS, C., TUSCHLING, K. & VON JUTERZENKA, K. 2002 The topography of the ice-water interface – its influence on the colonization of sea ice by algae. *Polar Biol.* **25**, 106–117.

NEUFELD, J. A. & WETTLAUFER, J. S. 2008 Shear-enhanced convection in a mushy layer. *J. Fluid Mech.* **612**, 339–361.

NEUFELD, J. A., WETTLAUFER, J. S., FELTHAM, D. L. & WORSTER, M. G. 2006 Corrigendum to flow-induced morphological instability of a mushy layer. *J. Fluid Mech.* **549**, 442–443.

PEPPIN, S. S. L., AUSSILLOUS, P., HUPPERT, H. E. & WORSTER, M. G. 2007 Steady-state mushy layers: experiments and theory. *J. Fluid Mech.* **570**, 69–77.

SARAZIN, J. R. & HELLAWELL, A. 1988 Channel formation in Pb-Sn, Pb-Sb, and Pb-Sn-Sb alloy ingots and comparison with the system NH_4Cl-H_2O. *Metall. Trans.* A **19**, 1861–1871.

TAIT, S. & JAUPART, C. 1989 Compositional convection in viscous melts. *Nature* **338**, 571–574.

TAIT, S. & JAUPART, C. 1992 Compositional convection in a reactive crystalline mush and melt differentiation. *J. Geophys. Res.* **97** (B5), 6735–6756.

VELLA, D. & WETTLAUFER, J. S. 2007 Finger rafting: a generic instability of floating elastic sheets. *Phys. Rev. Lett.* **98**, 088303.

WASHBURN, E. W. (Ed.) 2003 *International Critical Tables of Numerical Data, Physics, Chemistry and Technology*. Knovel.

WETTLAUFER, J. S., WORSTER, M. G. & HUPPERT, H. E. 1997*a* Natural convection during solidification of an alloy from above with application to the evolution of sea ice. *J. Fluid Mech.* **344**, 291–316.

WETTLAUFER, J. S., WORSTER, M. G. & HUPPERT, H. E. 1997*b* The phase evolution of young sea ice. *Geophys. Res. Lett.* **24**, 1251–1254.

WIDELL, K., FER, I. & HAUGAN, P. M. 2006 Salt release from warming sea ice. *Geophys. Res. Lett.* **33**, L12501, doi:10.1029/2006GL026262.

WORSTER, M. G. 1986 Solidification of an alloy from a cooled boundary. *J. Fluid Mech.* **167**, 481–501.

WORSTER, M. G. 1992*a* The dynamics of mushy layers. In *Interactive Dynamics of Convection and Solidification* (ed. S. H. Davis, H. E. Huppert, U. Müller, M. G. Worster), pp. 113–138. Kluwer.

WORSTER, M. G. 1992*b* Instabilities of the liquid and mushy regions during solidification of alloys. *J. Fluid Mech.* **237**, 649–669.

WORSTER, M. G. 2000 Solidification of fluids. In *Perspectives in Fluid Dynamics* (ed. G. K. Batchelor, H. K. Moffatt, & M. G. Worster), pp. 393–446. Cambridge University Press.

WORSTER, M. G. & KERR, R. C. 1994 The transient behaviour of alloys solidified from below prior to the formation of chimneys. *J. Fluid Mech.* **269**, 23–44.